



Universiteit Gent
Faculteit Wetenschappen
Vakgroep Fysica en Sterrenkunde

2 No title yet

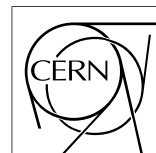
3 No sub-title neither, obviously...

4 Alexis Fagot

5



Thesis to obtain the degree of
Doctor of Philosophy in Physics
Academic years 2012-2017





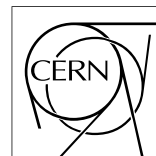
Universiteit Gent
Faculteit Wetenschappen
Vakgroep Fysica en Sterrenkunde

7
8 Promotoren: Dr. Michael Tytgat
Prof. Dr. Dirk Ryckbosch

9
10 Universiteit Gent
11 Faculteit Wetenschappen
12
13 Vakgroep Fysica en Sterrenkunde
14 Proeftuinstraat 86, B-9000 Gent, België
15 Tel.: +32 9 264.65.28
16 Fax.: +32 9 264.66.97



Thesis to obtain the degree of
Doctor of Philosophy in Physics
Academic years 2012-2017



Acknowledgements

19 Ici on remerciera tous les gens que j'ai pu croiser durant cette aventure et qui m'ont
20 permis de passer un bon moment

21 *Gent, ici la super date de la mort qui tue de la fin d'écriture*
22 *Alexis Fagot*

Table of Contents

24	Acknowledgements	i
25	Nederlandse samenvatting	xv
26	English summary	xvii
27	1 Introduction	1-1
28	1.1 A story of High Energy Physics	1-1
29	1.2 Organisation of this study	1-1
30	2 Investigating the TeV scale	2-1
31	2.1 The Standard Model of Particle Physics	2-1
32	2.2 The Large Hadron Collider and the Compact Muon Solenoid . . .	2-1
33	2.3 Muon Phase-II Upgrade	2-1
34	3 Amplification processes in gaseous detectors	3-1
35	3.1 Signal formation	3-1
36	3.2 Gas transport parameters	3-1
37	4 Resistive Plate Chambers	4-1
38	4.1 Principle	4-1
39	4.2 Rate capability of Resistive Plate Chambers	4-1
40	4.3 High time resolution	4-1
41	4.4 Resistive Plate Chambers at CMS	4-1
42	4.4.1 Overview	4-1
43	4.4.2 The present RPC system	4-2
44	4.4.3 Pulse processing of CMS RPCs	4-3
45	5 Longevity studies and Consolidation of the present CMS RPC subsystem	5-1
46	5.1 Testing detectors under extreme conditions	5-1
47	5.1.1 The Gamma Irradiation Facilities	5-2
48	5.1.1.1 GIF	5-2
49	5.1.1.2 GIF++	5-3
50	5.2 Preliminary tests at GIF	5-3
51	5.2.1 Resistive Plate Chamber test setup	5-3
52		

53	5.2.2	Data Acquisition	5-4
54	5.2.3	Geometrical acceptance of the setup layout to cosmic muons	5-4
55	5.2.3.1	Description of the simulation layout	5-5
56	5.2.3.2	Simulation procedure	5-5
57	5.2.3.3	Results	5-7
58	5.2.4	Photon flux at GIF	5-7
59	5.2.4.1	Expectations from simulations	5-7
60	5.2.4.2	Dose measurements	5-10
61	5.2.5	Results and discussions	5-10
62	5.3	Longevity tests at GIF++	5-11
63	5.3.1	Description of the Data Acquisition	5-12
64	5.3.2	RPC current, environmental and operation parameter mon-	
65		itoring	5-13
66	5.3.3	Measurement procedure	5-13
67	5.3.4	Longevity studies results	5-13
68	6	Investigation on high rate RPCs	6-1
69	6.1	Rate limitations and ageing of RPCs	6-1
70	6.1.1	Low resistivity electrodes	6-1
71	6.1.2	Low noise front-end electronics	6-1
72	6.2	Construction of prototypes	6-1
73	6.3	Results and discussions	6-1
74	7	Conclusions and outlooks	7-1
75	7.1	Conclusions	7-1
76	7.2	Outlooks	7-1
77	A	A data acquisition software for VME CAEN TDCs	A-1
78	A.1	Introduction	A-1
79	B	Details on the online analysis package	B-1
80	B.1	Introduction	B-1
81	C	Structure of the hybrid simulation software	C-1
82	C.1	Introduction	C-1

List of Figures

84	2.1	Absorbed dose in the CMS cavern after an integrated luminosity	
85		of 3000 fb. R is the transverse distance from the beamline and Z is	
86		the distance along the beamline from the Interaction Point at Z=0.	2-2
87	2.2	A quadrant of the muon system, showing DTs (yellow), RPCs	
88		(light blue), and CSCs (green). The locations of new forward	
89		muon detectors for Phase-II are contained within the dashed box	
90		and indicated in red for GEM stations (ME0, GE1/1, and GE2/1)	
91		and dark blue for improved RPC (iRPC) stations (RE3/1 and RE4/1).	2-3
92	2.3	RMS of the multiple scattering displacement as a function of muon	
93		p_T for the proposed forward muon stations. All of the electromag-	
94		netic processes such as bremsstrahlung and magnetic field effect	
95		are included in the simulation.	2-3
96	4.1	Signals from the RPC strips are shaped by the FEE described on	
97		Figure 4.1a. Output LVDS signals are then read-out by a TDC	
98		module connected to a computer or converted into NIM and sent	
99		to scalers. Figure 4.1b describes how these converted signals are	
100		put in coincidence with the trigger.	4-4
101	4.2	Description of the principle of a CFD. A comparison of threshold	
102		triggering (left) and constant fraction triggering (right) is shown	
103		in Figure 4.2a. Constant fraction triggering is obtained thanks to	
104		zero-crossing technique as explained in Figure 4.2b. The signal	
105		arriving at the input of the CFD is split into three components. A	
106		first one is delayed and connected to the inverting input of a first	
107		comparator. A second component is connected to the noninverting	
108		input of this first comparator. A third component is connected to	
109		the noninverting input of another comparator along with a thresh-	
110		old value connected to the inverting input. Finally, the output of	
111		both comparators is fed through an AND gate.	4-5
112	5.1	(5.1a) Extrapolation from 2016 data of single hit rate per unit area	
113		in the barrel region. (5.1b) Extrapolation from 2016 data of single	
114		hit rate per unit area in the endcap region.	5-14

115	5.2	Background Fluka simulation compared to 2016 Data at $L = 10^{34} \text{cm}^{-2} \cdot \text{s}^{-1}$	
116		in the fourth endcap disk region. A mismatch in between simula-	
117		tion and data can be observed. [To be understood.]	5-15
118	5.3	Layout of the test beam zone called X5c GIF at CERN. Photons	
119		from the radioactive source produce a sustained high rate of ran-	
120		dom hits over the whole area. The zone is surrounded by 8 m high	
121		and 80 cm thick concrete walls. Access is possible through three	
122		entry points. Two access doors for personnel and one large gate	
123		for material. A crane allows installation of heavy equipment in the	
124		area.	5-15
125	5.4	^{137}Cs decays by β^- emission to the ground state of ^{137}Ba (BR =	
126		5.64%) and via the 662 keV isomeric level of ^{137}Ba (BR = 94.36%)	
127		whose half-life is 2.55 min.	5-16
128	5.5	Floor plan of the GIF++ facility. When the facility downstream of	
129		the GIF++ takes electron beam, a beam pipe is installed along the	
130		beam line (z-axis). The irradiator can be displaced laterally (its	
131		center moves from $x = 0.65$ m to 2.15 m), to increase the distance	
132		to the beam pipe.	5-16
133	5.6	Simulated unattenuated current of photons in the xz plane (Fig-	
134		ure 5.6a) and yz plane (Figure 5.6b) through the source at $x = 0.65$ m	
135		and $y = 0$ m. With angular correction filters, the current of 662 keV	
136		photons is made uniform in xy planes.	5-17
137	5.7	Description of the RPC setup. Dimensions are given in mm. A	
138		tent containing RPCs is placed at 1720 mm from the source con-	
139		tainer. The source is situated in the center of the container. RE-	
140		4-2-BARC-161 chamber is 160 mm inside the tent. This way, the	
141		distance between the source and the chambers plan is 2060 mm.	
142		Figure 5.7a provides a side view of the setup in the xz plane while	
143		Figure 5.7b shows a top view in the yz plane.	5-18
144	5.8	RE-4-2-BARC-161 chamber is inside the tent as described in Fig-	
145		ure 5.7. In the top right, the two scintillators used as trigger can	
146		be seen. This trigger system has an inclination of 10° relative	
147		to horizontal and is placed above half-partition B2 of the RPCs.	
148		PMT electronics are shielded thanks to lead blocks placed in order	
149		to protect them without stopping photons from going through the	
150		scintillators and the chamber.	5-18

151	5.9	Hit distributions over all 3 parttions of RE-4-2-BARC-161 cham-	
152		ber is showed on these plots. Top, middle and bottom figures re-	
153		spectively correspond to partitions A, B, and C. These plots show	
154		that some events still occur in other half-partitions than B2, which	
155		corresponds to strips 49 to 64, in front of which the trigger is	
156		placed, contributing to the inefficiency of detection of cosmic muons.	
157		In the case of partitions A and C, the very low amount of data can	
158		be interpreted as noise. On the other hand, it is clear that a lit-	
159		tle portion of muons reach the half-partition B1, corresponding to	
160		strips 33 to 48.	5-19
161	5.10	Module V1190A <i>Trigger Matching Mode</i> timing diagram.	5-20
162	5.11	Results are derived from data taken on half-partition B2 only. On	
163		the 18 th of June 2014, data has been taken on chamber RE-2-	
164		BARC-161 at building 904 (Preveessin Site) with cosmic muons	
165		providing us a reference efficiency plateau of $(97.54 \pm 0.15)\%$ rep-	
166		resented by a black curve. A similar measurement has been done	
167		at GIF on the 21 st of July with the same chamber giving a plateau	
168		of $(78.52 \pm 0.94)\%$ represented by a red curve.	5-20
169	5.12	Representation of the layout used for the simulations of the test	
170		setup. The RPC is represented as a yellow trapezoid while the two	
171		scintillators as blue cuboids looking at the sky. A green plane cor-	
172		responds to the muon generation plane within the simulation. Fig-	
173		ure 5.7a shows a global view of the simulated setup. Figure 5.7b	
174		shows a zommed view that allows to see the 2 scintillators as well	
175		as the full RPC plane.	5-21
176	5.13	γ flux $F(D)$ is plot using values from table 5.1. As expected, the	
177		plot shows similar attenuation behaviours with increasing distance	
178		for each absorpion factors.	5-22
179	5.14	Figure 5.14a shows the linear approximation fit done via formu-	
180		lae 5.7 on data from table 5.2. Figure 5.14b shows a comparison	
181		of this model with the simulated flux using a and b given in fig-	
182		ure 5.14a in formulae 5.4 and the reference value $D_0 = 50cm$	
183		and the associated flux for each absorption factor F_0^{ABS} from ta-	
184		ble 5.1	5-23
185	5.15	Dose measurements has been done in a plane corresponding to the	
186		tents front side. This plan is 1900 mm away from the source. As	
187		explained in the first chapter, a lens-shaped lead filter provides a	
188		uniform photon flux in the vertical plan orthogonal to the beam	
189		direction. If the second line of measured fluxes is not taken into	
190		account because of lower values due to experimental equipments	
191		in the way between the source and the tent, the uniformity of the	
192		flux is well showed by the results.	5-24
193	5.16	5-24

194	5.17	Evolution of the maximum efficiency for RE2 (5.17a) and RE4	
195		(5.17b) chambers with increasing extrapolated γ rate per unit area	
196		at working point. Both irradiated (blue) and non irradiated (red)	
197		chambers are shown.	5-25
198	5.18	Evolution of the working point for RE2 (5.18a) and RE4 (5.18b)	
199		with increasing extrapolated γ rate per unit area at working point.	
200		Both irradiated (blue) and non irradiated (red) chambers are shown.	5-25
201	5.19	Evolution of the maximum efficiency at HL-LHC conditions, i.e.	
202		a background hit rate per unit area of 300 Hz/cm^2 , with increasing	
203		integrated charge for RE2 (5.19a) and RE4 (5.19b) detectors. Both	
204		irradiated (blue) and non irradiated (red) chambers are shown. The	
205		integrated charge for non irradiated detectors is recorded during	
206		test beam periods and stays small with respect to the charge accu-	
207		mulated in irradiated chambers.	5-26
208	5.20	Comparison of the efficiency sigmoid before (triangles) and after	
209		(circles) irradiation for RE2 (5.20a) and RE4 (5.20b) detectors.	
210		Both irradiated (blue) and non irradiated (red) chambers are shown.	5-26
211	5.21	Evolution of the Bakelite resistivity for RE2 (5.21a) and RE4 (5.21b)	
212		detectors. Both irradiated (blue) and non irradiated (red) chambers	
213		are shown.	5-27
214	5.22	Evolution of the noise rate per unit area for the irradiated chamber	
215		RE2-2-BARC-9 only.	5-27

List of Tables

217	5.1	Total photon flux ($E\gamma \leq 662$ keV) with statistical error predicted	
218		considering a ^{137}Cs activity of 740 GBq at different values of the	
219		distance D to the source along the x-axis of irradiation field [6]. . .	5-8
220	5.2	Correction factor c is computed thanks to formulae 5.5 taking as	
221		reference $D_0 = 50$ cm and the associated flux F_0^{ABS} for each ab-	
222		sorption factor available in table 5.1.	5-8
223	5.3	The data at D_0 in 1997 is taken from [6]. In a second step, using	
224		Equations 5.8 and 5.9, the flux at D can be estimated in 1997.	
225		Then, taking into account the attenuation of the source activity,	
226		the flux at D can be estimated at the time of the tests in GIF in	
227		2014. Finally, assuming a sensitivity of the RPC to γ $s = 2 \cdot 10^{-3}$,	
228		an estimation of the hit rate per unit area is obtained.	5-9

229

List of Acronyms

230

List of Acronyms

231

232

233

B

234

235 BARC
236 BR

Bhabha Atomic Research Centre
Branching Ratio

237

238

239

C

240

241 CAEN
242

Costruzioni Apparecchiature Elettroniche Nucleari S.p.A.

243 CERN
244 CFD

European Organization for Nuclear Research
Constant Fraction Discriminator

245 CMS
246 CSC

Compact Muon Solenoid
Cathode Strip Chamber

247

248

249

D

250

251 DAQ
252 DCS
253 DQM
254 DT

Data Acquisition
Detector Control Software
Data Quality Monitoring
Drift Tube

255

256

257

F

258

259 FEE

Front-End Electronics

260	FEB	Front-End Board
261		
262		
263	G	
264		
265	GE-/-	Find a good description
266	GE1/1	Find a good description
267	GE2/1	Find a good description
268	GEANT	GEometry ANd Tracking - a series of software toolkit
269		platforms developed by CERN
270	GEM	Gas Electron Multiplier
271	GIF	Gamma Irradiation Facility
272	GIF++	new Gamma Irradiation Facility
273		
274		
275	H	
276		
277	HL-LHC	High Luminosity LHC
278	HV	High Voltage
279		
280		
281	I	
282		
283	iRPC	improved RPC
284		
285		
286	L	
287		
288	LHC	Large Hadron Collider
289	LS1	First Long Shutdown
290	LS3	Third Long Shutdown
291	LV	Low Voltage
292	LVDS	Low-Voltage Differential Signaling
293		
294		
295	M	
296		
297	MC	Monte Carlo

298	MCNP	Monte Carlo N-Particle
299	ME-/-	Find good description
300	ME0	Find good description
301		
302		
303	N	
304		
305	NIM	Nuclear Instrumentation Module logic signals
306		
307		
308	P	
309		
310	PMT	PhotoMultiplier Tube
311		
312		
313	R	
314		
315	RE-/-	Find a good description
316	RE2/2	Find a good description
317	RE3/1	Find a good description
318	RE3/2	Find a good description
319	RE4/1	Find a good description
320	RE4/2	Find a good description
321	RE4/3	Find a good description
322	RMS	Root Mean Square
323	ROOT	a framework for data processing born at CERN
324	RPC	Resistive Plate Chamber
325		
326		
327	S	
328		
329	SPS	Super Proton Synchrotron
330		
331		
332	T	
333		
334	TDC	Time-to-Digital Converter

336

Nederlandse samenvatting –Summary in Dutch–

337

338 Le resume en Neerlandais (j'aurais peut-etre de apprendre la langue juste pour
339 ca...).

340

English summary

341 Le meme résumé mais en Anglais (on commencera par la hein!).

1

Introduction

342

343

344 **1.1 A story of High Energy Physics**

345 **1.2 Organisation of this study**

2

Investigating the TeV scale

2.1 The Standard Model of Particle Physics

2.2 The Large Hadron Collider and the Compact Muon Solenoid

2.3 Muon Phase-II Upgrade

After the more than two years lasting First Long Shutdown (LS1), the Large Hadron Collider (LHC) delivered its very first Run-II proton-proton collisions early 2015. LS1 gave the opportunity to the LHC and to the its experiments to undergo upgrades. The accelerator is now providing collisions at center-of-mass energy of 13 TeV and bunch crossing rate of 40 MHz, with a peak luminosity exceeding its design value. During the first and upcoming second LHC Long Shutdown, the Compact Muon Solenoid (CMS) detector is also undergoing a number of upgrades to maintain a high system performance [1].

From the LHC Phase-2 or High Luminosity LHC (HL-LHC) period onwards, i.e. past the Third Long Shutdown (LS3), the performance degradation due to integrated radiation as well as the average number of inelastic collisions per bunch crossing, or pileup, will rise substantially and become a major challenge for the LHC experiments, like CMS that are forced to address an upgrade program for Phase-II [2]. Simulations of the expected distribution of absorbed dose in the CMS detector under HL-LHC conditions, show in figure 5.15 that detectors placed close

to the beamline will have to withstand high irradiation, the radiation dose being of the order of a few tens of Gy.

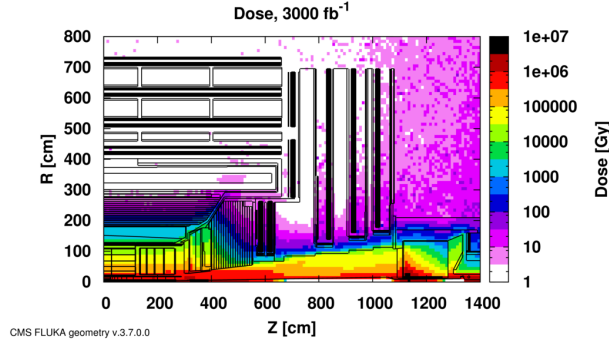


Figure 2.1: Absorbed dose in the CMS cavern after an integrated luminosity of 3000 fb. R is the transverse distance from the beamline and Z is the distance along the beamline from the Interaction Point at $Z=0$.

The measurement of small production cross-section and/or decay branching ratio processes, such as the Higgs boson coupling to charge leptons or the $B_s \rightarrow \mu^+ \mu^-$ decay, is of major interest and specific upgrades in the forward regions of the detector will be required to maximize the physics acceptance on the largest possible solid angle. To ensure proper trigger performance within the present coverage, the muon system will be completed with new chambers. In figure 2.2 one can see that the existing Cathode Strip Chambers (CSCs) will be completed by Gas Electron Multipliers (GEMs) and Resistive Plate Chambers (RPCs) in the pseudorapidity region $1.6 < |\eta| < 2.4$ to complete its redundancy as originally scheduled in the CMS Technical Proposal [3].

RPCs are used by the CMS first level trigger for their good timing performances. Indeed, a very good bunch crossing identification can be obtained with the present CMS RPC system, given their fast response of the order of 1 ns. In order to contribute to the precision of muon momentum measurements, muon chambers should have a spatial resolution less or comparable to the contribution of multiple scattering [1]. Most of the plausible physics is covered only considering muons with $p_T < 100$ GeV thus, in order to match CMS requirements, a spatial resolution of $\mathcal{O}(\text{few mm})$ the proposed new RPC stations, as shown by the simulation in figure 2.3. According to preliminary designs, RE3/1 and RE4/1 readout pitch will be comprised between 3 and 6 mm and 5 η -partitions could be considered.

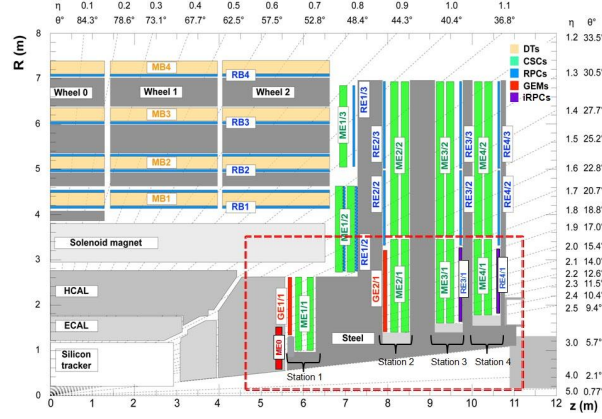


Figure 2.2: A quadrant of the muon system, showing DTs (yellow), RPCs (light blue), and CSCs (green). The locations of new forward muon detectors for Phase-II are contained within the dashed box and indicated in red for GEM stations (ME0, GE1/1, and GE2/1) and dark blue for improved RPC (iRPC) stations (RE3/1 and RE4/1).

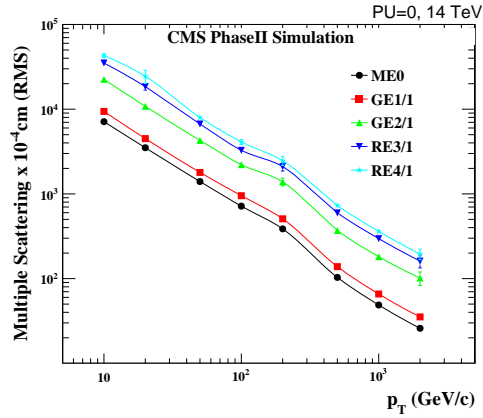


Figure 2.3: RMS of the multiple scattering displacement as a function of muon p_T for the proposed forward muon stations. All of the electromagnetic processes such as bremsstrahlung and magnetic field effect are included in the simulation.

3

389

390

Amplification processes in gaseous detectors

391

392

3.1 Signal formation

393

3.2 Gas transport parameters

4

Resistive Plate Chambers

4.1 Principle

4.2 Rate capability of Resistive Plate Chambers

4.3 High time resolution

4.4 Resistive Plate Chambers at CMS

4.4.1 Overview

The Resistive Plate Chambers (RPC) system, located in both barrel and endcap regions, provides a fast, independent muon trigger with a looser p_T threshold over a large portion of the pseudorapidity range ($|\eta| < 1.6$) [\[add reconstruction\]](#).

During High-Luminosity LHC (HL-LHC) operations the expected conditions in terms of background and pile-up will make the identification and correct P_T assignment a challenge for the Muon system. The goal of RPC upgrade is to provide additional hits to the Muon system with precise timing. All these informations will be elaborated by the trigger system in a global way enhancing the performance of the trigger in terms of efficiency and rate control. The RPC Upgrade is based on two projects: an improved Link Board System and the extension of the RPC coverage up to $|\eta| = 2.4$. [\[FIXME 2.4 or 2.5?\]](#)

413 The Link Board system, that will be described in section xxx, is responsible to
 414 process, synchronize and zero-suppress the signals coming from the RPC front end
 415 boards. The Link Board components have been produced between 2006 and 2007
 416 and will be subjected to aging and failure in the long term. The upgraded Link
 417 Board system will overcome the aging problems described in section xxx and will
 418 allow for a more precise timing information to the RPC hits from 25 to 1 ns [ref
 419 section xxx].

420 The extension of the RPC system up to $|\eta| = 2.1$ was already planned in the
 421 CMS TDR [ref cmstdr] and staged because of budget limitations and expected
 422 background rates higher than the rate capability of the present CMS RPCs in that
 423 region. An extensive R&D program has been done in order to develop an improved
 424 RPC that fulfills the CMS requirements. Two new RPC layers in the innermost ring
 425 of stations 3 and 4 will be added with benefits to the neutron-induced background
 426 reduction and efficiency improvement for both trigger and offline reconstruction.

427 4.4.2 The present RPC system

428 The RPC system is organized in 4 stations called RB1 to RB4 in the barrel region,
 429 and RE1 to RE4 in the endcap region. The innermost barrel stations, RB1 and
 430 RB2, are instrumented with 2 layers of RPCs facing the innermost (RB1in and
 431 RB2in) and outermost (RB1out and RB2out) sides of the DT chambers. Every
 432 chamber is then divided from the read-out point of view into 2 or 3 η partitions
 433 called “rolls”. The RPC system consist of 480 barrel chambers and 576 endcap
 434 chambers. Details on the geometry are discussed in the paper [ref to geo paper].

435 The CMS RPC chamber is a double-gap, operated in avalanche mode to ensure
 436 reliable operation at high rates. Each RPC gap consists of two 2-mm-thick resistive
 437 High-Pressure Laminate (HPL) plates separated by a 2-mm-thick gas gap. The
 438 outer surface of the HPL plates is coated with a thin conductive graphite layer, and
 439 a voltage is applied. The RPCs are operated with a 3-component, non-flammable
 440 gas mixture consisting of 95.2% freon ($C_2H_2F_4$, known as R134a), 4.5% isobutane
 441 ($i-C_4H_{10}$), and 0.3% sulphur hexafluoride (SF_6) with a relative humidity of 40% -
 442 50%. Readout strips are aligned in η between the 2 gas gaps. [\[Add a sentence on](#)
 443 [FEBS.\]](#)

444 The discriminated signals coming from the Front End boards feed via twisted
 445 cables (10 to 20 m long) the Link Board System located in UXC on the balconies
 446 around the detector. The Link System consist of the 1376 Link Boards (LBs)
 447 and the 216 Control Boards (CBs), placed in 108 Link Boxes. The Link Box
 448 is a custom crate (6U high) with 20 slots (for two CBs and eighteen LBs). The
 449 Link Box contains custom backplane to which the cables from the chambers are
 450 connected, as well as the cables providing the LBs and CBs power supply and the
 451 cables for the RPC FEBS control with use of the I2C protocol (through the CB). The

backplane itself contains only connectors (and no any other electronic devices).

The Link Board has 96 input channels (one channel corresponds to one RPC strip). The input signals are the ~ 100 ns binary pulses which are synchronous to the RPC hits, but not to the LHC clock (which drives the entire CMS electronics). Thus the first step of the FEB signals processing is synchronization, i.e. assignment of the signals to the BXes (25 ns periods). Then the data are compressed with a simple zero-suppressing algorithm (the input channels are grouped into 8 bit partitions, only the partitions with at least one nonzero bit are selected for each BX). Next, the non-empty partitions are time-multiplexed i.e. if there are more than one such partition in a given BX, they are sent one-by-one in consecutive BXes. The data from 3 neighbouring LBs are concentrated by the middle LB which contains the optical transmitter for sending them to the USC over a fiber at 1.6 Gbps.

The Control Boards provide the communication of the control software with the LBs via the FEC/CCU system. The CBs are connected into token rings, each ring consists of 12 CBs of one detector tower and a FEC mezzanine board placed on the CCS board located in the VME crate in the USC. In total, there are 18 rings in the entire Link System. The CBs also perform automatic reloading of the LB's firmware which is needed in order to avoid accumulation of the radiation induced SEUs in the LBs firmware.

Both LBs and CB are based on the Xilinx Spartan III FPGAs, the CB additionally contains radiation-tolerant (FLASH based) FPGA Actel ProAsicPlus.

The High Voltage power system is located in USC, not exposed to radiation and easily accessible for any reparation. A single HV channel powers 2 RPC chambers both in the barrel and endcap regions. The Low Voltage boards are located in UXC on the balconies and provide the voltage to the front end electronics.

4.4.3 Pulse processing of CMS RPCs

Signals induced by cosmic particle in the RPC strips are shaped by standard CMS RPC Front-End Electronics (FEE) following the scheme of Figure 4.1. On a first stage, analogic signals are amplified and then sent to the Constant Fraction Discriminator (CFD) described in Figure 4.2. At the end of the chain, 100 ns long pulses are sent in the LVDS output. These output signal are sent on one side to a V1190A Time-to-Digital Converter (TDC) module from CAEN and on the other to an OR module to count the number of detected signals. Trigger and hit coincidences are monitored using scalers. The TDC is used to store the data into ROOT files. These files are thus analysed to understand the detectors performance.

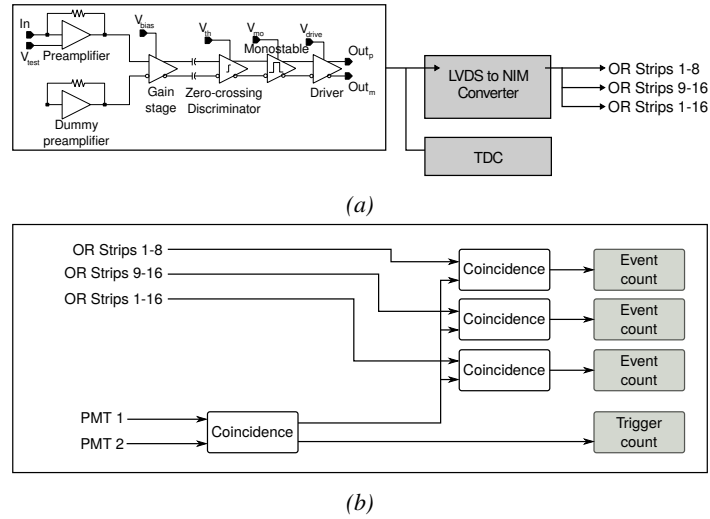


Figure 4.1: Signals from the RPC strips are shaped by the FEE described on Figure 4.1a. Output LVDS signals are then read-out by a TDC module connected to a computer or converted into NIM and sent to scalars. Figure 4.1b describes how these converted signals are put in coincidence with the trigger.

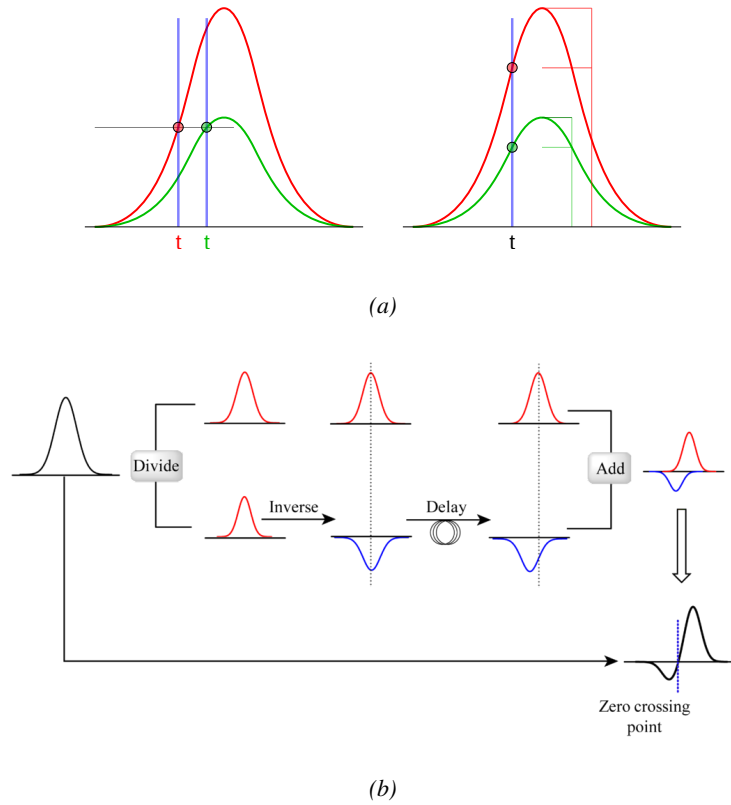


Figure 4.2: Description of the principle of a CFD. A comparison of threshold triggering (left) and constant fraction triggering (right) is shown in Figure 4.2a. Constant fraction triggering is obtained thanks to zero-crossing technique as explained in Figure 4.2b. The signal arriving at the input of the CFD is split into three components. A first one is delayed and connected to the inverting input of a first comparator. A second component is connected to the noninverting input of this first comparator. A third component is connected to the noninverting input of another comparator along with a threshold value connected to the inverting input. Finally, the output of both comparators is fed through an AND gate.

5

487

488 Longevity studies and Consolidation of 489 the present CMS RPC subsystem

490 5.1 Testing detectors under extreme conditions

491 The upgrade from LHC to HL-LHC will increase the peak luminosity from 10^{34}
492 $\text{cm}^{-2} \text{s}^{-1}$ to reach $5 \times 10^{34} \text{cm}^{-2} \text{s}^{-1}$, increasing in the same way the total ex-
493 pected background to which the RPC system will be subjected to. Composed of
494 low energy gammas and neutrons from p - p collisions, low momentum primary
495 and secondary muons, puch-through hadrons from calorimeters, and particles pro-
496 duced in the interaction of the beams with collimators, the background will mostly
497 affect the regions of CMS that are the closest to the beam line, i.e. the RPC detec-
498 tors located in the endcaps. [\[To update.\]](#)

499

500 The 2016 data allowed to study the values of the background rate in all RPC
501 system. In Figure 5.1, the distribution of the chamber background hit rate per unit
502 area is shown at a luminosity of $5 \times 10^{34} \text{cm}^{-2} \cdot \text{s}^{-1}$ linearly extrapolating from
503 data collected in 2016 [\[ref mentioning the linear dependency of rate vs lumi\]](#). The
504 maximum rate per unit area at HL-LHC conditions is expected to be of the or-
505 der of $600 \text{Hz}/\text{cm}^2$ (including a safety factor 3). Nevertheless, Fluka simulations
506 have conducted in order to understand the background at HL-LHC conditions. The
507 comparison to the data has shown, in Figure 5.2, a discrepancy of a factor 2 even
508 though the order of magnitude is consistent. [\[Understand mismatch.\]](#)

509

In the past, extensive long-term tests were carried out at several gamma and neutron facilities certifying the detector performance. Both full size and small prototype RPCs have been irradiated with photons up to an integrated charge of $\sim 0.05C/cm^2$ and $\sim 0.4C/cm^2$, respectively [4, 5]. During Run-I, the RPC system provided stable operation and excellent performance and did not show any aging effects for integrated charge of the order of $0.01C/cm^2$. Projections on currents from 2016 Data, has allowed to determine that the total integrated charge, by the end of HL-LHC, would be of the order of $1C/cm^2$ (including a safety factor 3). [\[Corresponding figure needed.\]](#)

5.1.1 The Gamma Irradiation Facilities

5.1.1.1 GIF

Located in the SPS West Area at the downstream end of the X5 test beam, the Gamma Irradiation Facility (GIF) was a test area in which particle detectors were exposed to a particle beam in presence of an adjustable gamma background [6]. Its goal was to reproduce background conditions these detectors would suffer in their operating environment at LHC. GIF layout is shown in Figure 5.3. Gamma photons are produced by a strong ^{137}Cs source installed in the upstream part of the zone inside a lead container. The source container includes a collimator, designed to irradiate a $6 \times 6 \text{ m}^2$ area at 5 m maximum to the source. A thin lens-shaped lead filter helps providing with a uniform outcoming flux in a vertical plane, orthogonal to the beam direction. The principal collimator hole provides a pyramidal aperture of $74^\circ \times 74^\circ$ solid angle and provides a photon flux in a pyramidal volume along the beam axis. The photon rate is controled by further lead filters allowing the maximum rate to be limited and to vary within a range of four orders of magnitude. Particle detectors under test are then placed within the pyramidal volume in front of the source, perpendicularly to the beam line in order to profit from the homogeneous photon flux. Adjusting the background flux of photons can then be done by using the filters and choosing the position of the detectors with respect to the source.

As described on Figure 5.4, the ^{137}Cs source emits a 662 keV photon in 85% of the decays. An activity of 740 GBq was measured on the 5th March 1997. To estimate the strength of the flux in 2014, it is necessary to consider the nuclear decay through time assiciated to the Cesium source whose half-life is well known ($t_{1/2} = (30.05 \pm 0.08) \text{ y}$). The GIF tests where done in between the 20th and the 31st of August 2014, i.e. at a time $t = (17.47 \pm 0.02) \text{ y}$ resulting in an attenuation of the activity from 740 GBq in 1997 to 494 GBq in 2014.

549 **5.1.1.2 GIF++**

550 The new Gamma Irradiation Facility (GIF++), located in the SPS North Area at
 551 the downstream end of the H4 test beam, has replaced its predecessor during LS1
 552 and has been operational since spring 2015 [7]. Like GIF, GIF++ features a ^{137}Cs
 553 source of 662 keV gamma photons, their fluence being controlled with a set of
 554 filters of various attenuation factors. The source provides two separated large irra-
 555 diation areas for testing several full-size muon detectors with continuous homoge-
 556 neous irradiation, as presented in Figure 5.5.

557
 558 The source activity was measured to be about 13.5 TBq in March 2016. The
 559 photon flux being far greater than HL-LHC expectations, GIF++ provides an ex-
 560 cellent facility for accelerated aging tests of muon detectors.

561
 562 The source is situated in the muon beam line with the muon beam being avail-
 563 able a few times a year. The H4 beam, composed of muons with a momentum of
 564 about 150 GeV/c, passes through the GIF++ zone and is used to study the per-
 565 formance of the detectors. Its flux is of 104 particles/s/cm² focused in an area
 566 similar to $10 \times 10 \text{ cm}^2$. Therefore, with properly adjusted filters, one can imitate
 567 the HL-LHC background and study the performance of muon detectors with their
 568 trigger/readout electronics in HL-LHC environment.

570 **5.2 Preliminary tests at GIF**

571 **5.2.1 Resistive Plate Chamber test setup**

572 During summer 2014, preliminary tests have been conducted in the GIF area on
 573 a newly produced RE4/2 chamber labelled RE-4-2-BARC-161. This chamber has
 574 been placed into a trolley covered with a tent. The position of the RPC inside the
 575 tent and of the tent related to the source is described in Figure 5.7. To test this
 576 CMS RPC, three different absorber settings were used. First of all, measurements
 577 were done with fully opened source. Then, to complete this preliminary study,
 578 the gamma flux has been attenuated from a factor 2 and a factor 5. The expected
 579 gamma flux at the level of our detector will be discussed in subsection 5.2.4.

580 At the time of the tests, the beam not being operationnal anymore, a trigger
 581 composed of 2 plastic scintillators has been placed in front of the setup with an
 582 inclination of 10 deg with respect to the detector plane in order to look at cosmic
 583 muons. Using this particular trigger layout, shown on Figure 5.8, leads to a cosmic
 584 muon hit distribution into the chamber similar to the one in Figure 5.9. Measured
 585 without gamma irradiation, two peaks can be seen on the profil of partition B, centered
 586 on strips 52 and 59. Section 5.2.3 will help us undertand that these two peaks

are due respectively to forward and backward coming cosmic particles where forward coming particles are first detected by the scintillators and then the RPC while the backward coming muons are first detected in the RPC.

5.2.2 Data Acquisition

As previously described in Section 4.4.3, CMS RPC FEEs provide us with 100 ns long LVDS output signals. These signals are then sent into V1190A Time-to-Digital Converter (TDC) modules manufactured by CAEN [8]. V1190A are VME units accepting 128 independent Multi-Hit/Multi-Event TDC channels whose signals are treated by 4 100 ps high performance TDC chips, developed by CERN/ECP-MIC Division. The data acquisition used at GIF takes profit of the *Trigger Matching Mode* offered by modules V1190A. A trigger matching is performed in between a trigger time tag and the channel time measurements. The signal provided by the coincidence of both PMTs is used to trigger the data acquisition. Control over this data acquisition mode, explained through Figure 5.10 is offered through 4 programmable parameters:

- **match window:** the match between a trigger and a hit is done within a programmable time window
- **window offset:** temporal distance between the trigger tag and the start of the trigger matching window
- **extra search margin:** an extended time window is used to ensure that all matching hits are found
- **reject margin:** older hits are automatically rejected to prevent buffer overflows and to speed up the search time

5.2.3 Geometrical acceptance of the setup layout to cosmic muons

In order to profit from a constant gamma irradiation, the detectors inside of the GIF bunker need to be placed in a plane orthogonal to the beam line. The muon beam that used to be available was meant to test the performance of detectors under test. This beam not being active anymore, another solution to test detector performance had to be used. Thus, it has been decided to use cosmic muons detected through a telescope composed of two scintillators. Lead blocks were used as shielding to protect the photomultipliers from gammas as can be seen from Figure 5.8.

An inclination has been given to the cosmic telescope to maximize the muon flux. A good compromise had to be found between good enough muon flux and narrow enough hit distribution to be sure to contain all the events into only one half partitions as required from the limited available readout hardware. Nevertheless,

a consequence of the misplaced trigger, that can be seen as a loss of events in half-partition B1 in Figure 5.9, is an inefficiency. Nevertheless, the inefficiency of approximately 20 % highlighted in Figure 5.11 by comparing the performance of chamber BARC-161 in 904 and at GIF without irradiation seems too important to be explained only by the geometrical acceptance of the setup itself. Simulations have been conducted to show how the setup brings inefficiency.

5.2.3.1 Description of the simulation layout

The layout of GIF setup has been reproduced and incorporated into a Monte Carlo (MC) simulation to study the influence of the disposition of the telescope on the final distribution measured by the RPC. A 3D view of the simulated layout is given into Figure 5.12. Muons are generated randomly in a horizontal plane located at a height corresponding to the lowest point of the PMTs. This way, the needed size of the plane in order to simulate events happening at very big azimuthal angles (i.e. $\theta \approx \pi$) can be kept relatively small. The muon flux is designed to follow the usual $\cos^2\theta$ distribution for cosmic particle. The goal of the simulation is to look at muons that pass through the muon telescope composed of the two scintillators and define their distribution onto the RPC plane. During the reconstruction, the RPC plane is then divided into its strips and each muon track is assigned to a strip.

In order to further refine the quality of the simulation and understand deeper the results the dependance of the distribution has been studied for a range of telescope inclinations. Moreover, the threshold applied on the PMT signals has been included into the simulation in the form of a cut. In the approximation of uniform scintillators, it has been considered that the threshold can be understood as the minimum distance particles need to travel through the scintillating material to give a strong enough signal. Particles that travel a distance smaller than the set "threshold" are thus not detected by the telescope and cannot trigger the data taking. Finally, the FEE threshold also has been considered in a similar way. The mean momentum of horizontal cosmic rays is higher than those of vertical ones but the stopping power of matter for momenta ranging from 1 GeV to 1 TeV stays comparable. It is then possible to assume that the mean number of primary e^-/ion pairs per unit length will stay similar and thus, depending on the applied discriminator threshold, muons with the shortest path through the gas volume will deposit less charge and induce a smaller signal on the pick-up strips that could eventually not be detected. These two thresholds also restrain the overall geometrical acceptance of the system.

5.2.3.2 Simulation procedure

The simulation software has been designed using C++ and the output data is saved into ROOT histograms. Simulations start for a threshold T_{scint} varying in a range

from 0 to 45 mm in steps of 5 mm, where $T_{scint} = 0$ mm corresponds to the case where there isn't any threshold apply on the input signal while $T_{scint} = 45$ mm, which is the scintillator thickness, is the case where muons cannot arrive orthogonally onto the scintillator surface. For a given T_{scint} , a set of RPC thresholds are considered. The RPC threshold, T_{RPC} varies from 2 mm, the thickness of the gas volume, to 3 mm in steps of 0.25 mm. For each $(T_{scint}; T_{RPC})$ pair, $N_\mu = 10^8$ muons are randomly generated inside the muon plane described in the previous paragraph with an azimuthal angle θ chosen to follow a $\cos^2\theta$ distribution.

Planes are associated to each surface of the scintillators. Knowing muon position into the muon plane and its direction allows us, by assuming that muons travel in a straight line, to compute the intersection of the muon track with these planes. Applying conditions to the limits of the surfaces of the scintillator faces then gives us an answer to whether or not the muon passed through the scintillators. In the case the muon has indeed passed through the telescope, the path through each scintillator is computed and muons whose path was shorter than T_{scint} are rejected and are thus considered as having not interacted with the setup.

On the contrary, if the muon is labeled as good, its position within the RPC plane is computed and the corresponding strip, determined by geometrical tests in the case the distance through the gas volume was enough not to be rejected because of T_{RPC} , gets a hit and several histograms are filled in order to keep track of the generation point on the muon plane, the intersection points of the reconstructed muons within the telescope, or on the RPC plane, the path traveled through each individual scintillator or the gas volume, as well as other histograms. Moreover, muons fill different histograms whether they are forward or backward coming muons. They are discriminated according to their direction components. When a muon is generated, an (x, y, z) position is assigned into the muon plane as well as a $(\theta; \phi)$ pair that gives us the direction it's coming from. This way, muons satisfying the condition $0 \leq \phi < \pi$ are designated as backward coming muons while muons satisfying $\pi \leq \phi < 2\pi$ as forward coming muons.

This simulation is then repeated for different telescope inclinations ranging in between 4 and 20° and varying in steps of 2°. Due to this inclination and to the vertical position of the detector under test, the muon distribution reconstructed in the detector plane is asymmetrical. The choice as been made to chose a skew distribution formula to fit the data built as the multiplication of gaussian and sigmoidal curves together. A typical gaussian formula is given as 5.1 and has three free parameters as A_g , its amplitude, \bar{x} , its mean value and σ , its root mean square. Sigmoidal curves as given by formula 5.2 are functions converging to 0 and A_s as x diverges. The inflexion point is given as x_i and λ is proportional to the slope at $x = x_i$. In the limit where $\lambda \rightarrow \infty$, the sigmoid becomes a step function.

$$g(x) = A_g e^{\frac{-(x-\bar{x})^2}{2\sigma^2}} \quad (5.1)$$

$$s(x) = \frac{A_s}{1 + e^{-\lambda(x-x_i)}} \quad (5.2)$$

699 Finally, a possible representation of a skew distribution is given by formula 5.3
 700 and is the product of 5.1 and 5.2. Naturally, here $A_{sk} = A_g \times A_s$ and represents
 701 the theoretical maximum in the limit where the skew tends to a gaussian function.

$$sk(x) = g(x) \times s(x) = A_{sk} \frac{e^{\frac{-(x-\bar{x})^2}{2\sigma^2}}}{1 + e^{-\lambda(x-x_i)}} \quad (5.3)$$

702 5.2.3.3 Results

703 **Influence of T_{scint} on the muon distribution**

704 **Influence of T_{RPC} on the muon distribution**

705 **Influence of the telescope inclination on the muon distribution**

706 **Comparison to data taken at GIF without irradiation**

707 5.2.4 Photon flux at GIF

708 5.2.4.1 Expectations from simulations

709 In order to understand and evaluate the γ flux in the GIF area, simulations had been
 710 conducted in 1999 and published by S. Agosteo et al [6]. Table 5.1 presented in
 711 this article gives us the γ flux for different distances D to the source. This sim-
 712 ulation was done using GEANT and a Monte Carlo N-Particle (MCNP) transport
 713 code, and the flux F is given in number of γ per unit area and unit time along with
 714 the estimated error from these packages expressed in %.

715 The simulation doesn't directly provides us with an estimated flux at the level
 716 of our RPC. First of all, it is needed to extract the value of the flux from the
 717 available data contained in the original paper and then to estimate the flux in 2014
 718 at the time the experimentation took place. Figure 5.13 that contains the data from
 719 Table 5.1. In the case of a pointlike source emitting isotrope and homogeneous
 720 gamma radiations, the gamma flux F at a distance D to the source with respect
 721 to a reference point situated at D_0 where a known flux F_0 is measured will be

Nominal ABS	Photon flux F [$\text{s}^{-1}\text{cm}^{-2}$]			
	at $D = 50$ cm	at $D = 155$ cm	at $D = 300$ cm	at $D = 400$ cm
1	$0.12 \cdot 10^8 \pm 0.2\%$	$0.14 \cdot 10^7 \pm 0.5\%$	$0.45 \cdot 10^6 \pm 0.5\%$	$0.28 \cdot 10^6 \pm 0.5\%$
2	$0.68 \cdot 10^7 \pm 0.3\%$	$0.80 \cdot 10^6 \pm 0.8\%$	$0.25 \cdot 10^6 \pm 0.8\%$	$0.16 \cdot 10^6 \pm 0.6\%$
5	$0.31 \cdot 10^7 \pm 0.4\%$	$0.36 \cdot 10^6 \pm 1.2\%$	$0.11 \cdot 10^6 \pm 1.2\%$	$0.70 \cdot 10^5 \pm 0.9\%$

Table 5.1: Total photon flux ($E\gamma \leq 662$ keV) with statistical error predicted considering a ^{137}Cs activity of 740 GBq at different values of the distance D to the source along the x -axis of irradiation field [6].

expressed like in Equation 5.4, assuming that the flux decreases as $1/D^2$, where c is a fitting factor.

$$F^{ABS} = F_0^{ABS} \times \left(\frac{cD_0}{D} \right)^2 \quad (5.4)$$

By rewriting Equation 5.4, it comes that :

$$c = \frac{D}{D_0} \sqrt{\frac{F^{ABS}}{F_0^{ABS}}} \quad (5.5)$$

$$\Delta c = \frac{c}{2} \left(\frac{\Delta F^{ABS}}{F^{ABS}} + \frac{\Delta F_0^{ABS}}{F_0^{ABS}} \right) \quad (5.6)$$

Finally, using Equation 5.5 and the data in Table 5.1 with $D_0 = 50$ cm as reference point, we can build Table 5.2. It is interesting to note that c for each value of D doesn't depend on the absorption factor.

Nominal ABS	Correction factor c		
	at $D = 155$ cm	at $D = 300$ cm	at $D = 400$ cm
1	$1.059 \pm 0.70\%$	$1.162 \pm 0.70\%$	$1.222 \pm 0.70\%$
2	$1.063 \pm 1.10\%$	$1.150 \pm 1.10\%$	$1.227 \pm 0.90\%$
5	$1.056 \pm 1.60\%$	$1.130 \pm 1.60\%$	$1.202 \pm 1.30\%$

Table 5.2: Correction factor c is computed thanks to formulae 5.5 taking as reference $D_0 = 50$ cm and the associated flux F_0^{ABS} for each absorption factor available in table 5.1.

For the range of D/D_0 values available, it is possible to use a simple linear fit to get the evolution of c . The linear fit will then use only 2 free parameters, a and b , as written in Equation 5.7. This gives us the results showed in Figure 5.14. Figure 5.14b confirms that using only a linear fit to extract c is enough as the evolution of the rate that can be obtained superimposes well on the simulation points.

$$c\left(\frac{D}{D_0}\right) = a\frac{D}{D_0} + b \quad (5.7)$$

$$F^{ABS} = F_0^{ABS} \left(a + \frac{bD_0}{D}\right)^2 \quad (5.8)$$

$$\Delta F^{ABS} = F^{ABS} \left[\frac{\Delta F_0^{ABS}}{F_0^{ABS}} + 2 \frac{\Delta a + \Delta b \frac{D_0}{D}}{a + \frac{bD_0}{D}} \right] \quad (5.9)$$

In the case of the 2014 GIF tests, the RPC plane is located at a distance $D = 206$ cm to the source. Moreover, to estimate the strength of the flux in 2014, it is necessary to consider the nuclear decay through time associated to the Cesium source whose half-life is well known ($t_{1/2} = (30.05 \pm 0.08)$ y). The very first source activity measurement has been done on the 5th of March 1997 while the GIF tests were done in between the 20th and the 31st of August 2014, i.e. at a time $t = (17.47 \pm 0.02)$ y resulting in an attenuation of the activity from 740 GBq in 1997 to 494 GBq in 2014. All the needed information to extrapolate the flux through our detector in 2014 has now been assembled, leading to the Table 5.3. It is interesting to note that for a common RPC sensitivity to γ of $2 \cdot 10^{-3}$, the order of magnitude of the estimated hit rate per unit area is of the order of the kHz for the fully opened source. Moreover, taking profit of the two working absorbers, it will be possible to scan background rates at 0 Hz, ~ 300 Hz as well as ~ 600 Hz. Without source, a good estimate of the intrinsic performance will be available. Then at 300 Hz, the goal will be to show that the detectors fulfill the performance certification of CMS RPCs. Then a first idea of the performance of the detectors at higher background will be provided with absorption factors 2 (~ 600 Hz) and 1 (no absorption). *[Here I will also put a reference to the plot showing the estimated background rate at the level of RE3/1 in the case of HL-LHC but this one being in another chapter, I will do it later.]*

Nominal ABS	Photon flux F [$\text{s}^{-1}\text{cm}^{-2}$]			Hit rate/unit area [Hz cm^{-2}] at $D^{2014} = 206$ cm
	at $D_0^{1997} = 50$ cm	at $D^{1997} = 206$ cm	at $D^{2014} = 206$ cm	
1	$0.12 \cdot 10^8 \pm 0.2\%$	$0.84 \cdot 10^6 \pm 0.3\%$	$0.56 \cdot 10^6 \pm 0.3\%$	1129 ± 32
2	$0.68 \cdot 10^7 \pm 0.3\%$	$0.48 \cdot 10^6 \pm 0.3\%$	$0.32 \cdot 10^6 \pm 0.3\%$	640 ± 19
5	$0.31 \cdot 10^7 \pm 0.4\%$	$0.22 \cdot 10^6 \pm 0.3\%$	$0.15 \cdot 10^6 \pm 0.3\%$	292 ± 9

Table 5.3: The data at D_0 in 1997 is taken from [6]. In a second step, using Equations 5.8 and 5.9, the flux at D can be estimated in 1997. Then, taking into account the attenuation of the source activity, the flux at D can be estimated at the time of the tests in GIF in 2014. Finally, assuming a sensitivity of the RPC to γ $s = 2 \cdot 10^{-3}$, an estimation of the hit rate per unit area is obtained.

754 **5.2.4.2 Dose measurements**

755 **5.2.5 Results and discussions**

5.3 Longevity tests at GIF++

Longevity studies imply a monitoring of the performance of the detectors probed using a high intensity muon beam in a irradiated environment by periodically measuring their rate capability, the dark current running through them and the bulk resistivity of the Bakelite composing their electrodes. GIF++, with its very intense ^{137}Cs source, provides the perfect environment to perform such kind of tests. Assuming a maximum acceleration factor of 3, it is expected to accumulate the equivalent charge in 1.7 years.

As the maximum background is found in the endcap, the choice naturally was made to focus the GIF++ longevity studies on endcap chambers. Most of the RPC system was installed in 2007. Nevertheless, the large chambers in the fourth endcap (RE4/2 and RE4/3) have been installed during LS1 in 2014. The Bakelite of these two different productions having different properties, four spare chambers of the present system were selected, two RE2,3/2 spares and two RE4/2 spares. Having two chambers of each type allows to always keep one of them non irradiated as reference, the performance evolution of the irradiated chamber being then compared through time to the performance of the non irradiated one.

The performance of the detectors under different level of irradiation is measured periodically during dedicated test beam periods using the H4 muon beam. In between these test beam periods, the two RE2,3/2 and RE4/2 chambers selected for this study are irradiated by the ^{137}Cs source in order to accumulate charge and the gamma background is monitored, as well as the currents. The two remaining chambers are kept non-irradiated as reference detectors. Due to the limited gas flow in GIF++, the RE4 chamber remained non-irradiated until end of November 2016 where a new mass flow controller has been installed allowing for bigger volumes of gas to flow in the system.

Figures 5.17 and 5.18 give us for different test beam periods, and thus for increasing integrated charge through time, a comparison of the maximum efficiency, obtained using a sigmoid-like function, and of the working point of both irradiated and non irradiated chambers [9]. No aging is yet to see from this data, the shifts in γ rate per unit area in between irradiated and non irradiated detectors and RE2 and RE4 types being easily explained by a difference of sensitivity due to the various Bakelite resistivities of the HPL electrodes used for the electrode production.

Collecting performance data at each test beam period allows us to extrapolate the maximum efficiency for a background hit rate of 300 Hz/cm^2 corresponding to the expected HL-LHC conditions. Aging effects could emerge from a loss of efficiency with increasing integrated charge over time, thus Figure 5.19 helps us understand such degradation of the performance of irradiated detectors in comparison with non irradiated ones. The final answer for an eventual loss of efficiency is given in Figure 5.20 by comparing for both irradiated and non irradiated detectors

the efficiency sigmoids before and after the longevity study. Moreover, to complete the performance information, the Bakelite resistivity is regularly measured thanks to Ag scans (Figure 5.21) and the noise rate is monitored weekly during irradiation periods (Figure 5.22). At the end of 2016, no signs of aging were observed and further investigation is needed to get closer to the final integrated charge requirements proposed for the longevity study of the present CMS RPC sub-system.

5.3.1 Description of the Data Acquisition

For the longevity studies, four spare chambers of the present system are used. Two spare RPCs of the RE2,3 stations as well as two spare RPCs from the new RE4 stations have been mounted in a Trolley. Six RE4 gaps are also placed in the trolley. The trolley is placed inside the GIF++ in the upstream region of the bunker, taking the cesium source as a reference. The trolley is oriented for the detection surface of the chambers to be orthogonal to the beam line. The system can be moved along the orthogonal plane in order to have the beam in all η -partitions. For the aging the trolley is moved outside the beam line and is placed in a distance of 5.2 m to the source, which irradiates the bunker using an attenuation filter of 2.2 which corresponds to a fluence of 10^7 gamma/cm^2 .

During GIF++ operation, the data collected can be divided into different categories as several parameters are monitored in addition to the usual RPC performance data. On one hand, to know the performance of a chamber, it is need to measure its efficiency and to know the background conditions in which it is operated. To do this, the hit signals from the chamber are recorded and stored in a ROOT file via a Data Acquisition (DAQ) software. On the other hand, it is also very important to monitor parameters such as environmental pressure and temperature, gas temperature and humidity, RPC HV, LV, and currents, or even source and beam status. This is done through the GIF++ web Detector Control Software (DCS) that stores this information in a database.

Two different types of tests are conducted on RPCs via the DAQ. Indeed, the performance of the detectors is measured periodically during dedicated test beam periods using the H4 muon beam. In between these test beam periods, when the beam is not available, the chambers are irradiated by the ^{137}Cs in order to accumulate deposited charge and the gamma background is measured.

RPCs under test are connected through LVDS cables to V1190A Time-to-Digital Converter (TDC) modules manufactured by CAEN. These modules, located in the rack area outside of the bunker, get the logic signals sent by the chambers and save them into their buffers. Due to the limited size of the buffers, the collected data is regularly erased and replaced. A trigger signal is needed for the TDC modules to send the useful data to the DAQ computer via a V1718 CAEN

835 USB communication module.

836 In the case of performance test, the trigger signal used for data acquisition is
 837 generated by the coincidence of three scintillators. A first one is placed upstream
 838 outside of the bunker, a second one is placed downstream outside of the bunker,
 839 while a third one is placed in front of the trolley, close by the chambers. Every time
 840 a trigger is sent to the TDCs, i.e. every time a muon is detected, knowing the time
 841 delay in between the trigger and the RPC signals, signals located in the right time
 842 window are extracted from the buffers and saved for later analysis. Signals are
 843 taken in a time window of 400 ns centered on the muon peak (here we could show
 844 a time spectrum). On the other hand, in the case of background rate measurement,
 845 the trigger signal needs to be "random" not to measure muons but to look at gamma
 846 background. A trigger pulse is continuously generated at a rate of 300 Hz using a
 847 dual timer. To integrate an as great as possible time, all signals contained within
 848 a time window of 10us prior to the random trigger signal are extracted from the
 849 buffers and saved for further analysis (here another time spectrum to illustrate
 850 could be useful, maybe even place both spectrum together as a single Figure).

851 The signals sent to the TDCs correspond to hit collections in the RPCs. When a
 852 particle hits a RPC, it induce a signal in the pickup strips of the RPC readout. If this
 853 signal is higher than the detection threshold, a LVDS signal is sent to the TDCs.
 854 The data is then organised into 4 branches keeping track of the event number, the
 855 hit multiplicity for the whole setup, and the time and channel profile of the hits in
 856 the TDCs.

857 **5.3.2 RPC current, environmental and operation parameter mon-** 858 **itoring**

859 In order to take into account the variation of pressure and temperature between
 860 different data taking periods the applied voltage is corrected following the rela-
 861 tionship :

$$HV_{eff} = HV_{app} \times \left(0.2 + 0.8 \cdot \frac{P_0}{P} \times \frac{T}{T_0} \right) \quad (5.10)$$

862 where T_0 (=293 K) and P_0 (=990 mbar) are the reference values.

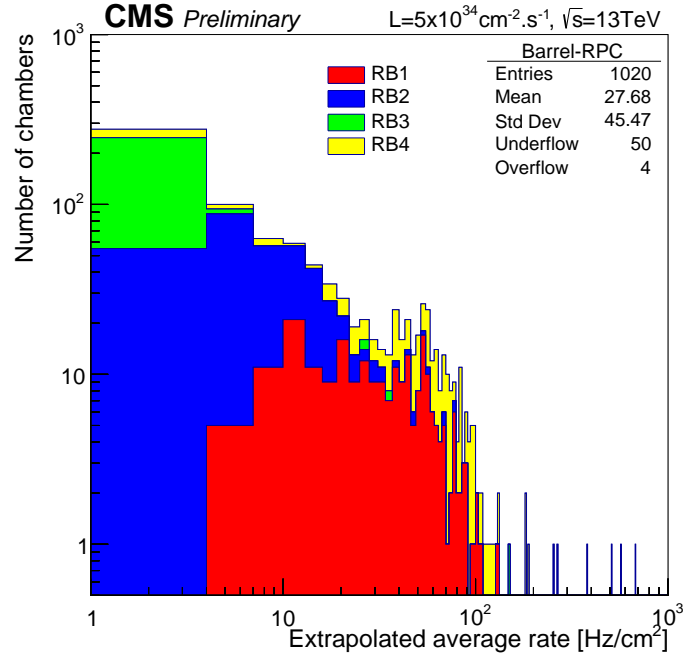
863 **5.3.3 Measurement procedure**

864 Insert a short description of the online tools (DAQ, DCS, DQM).

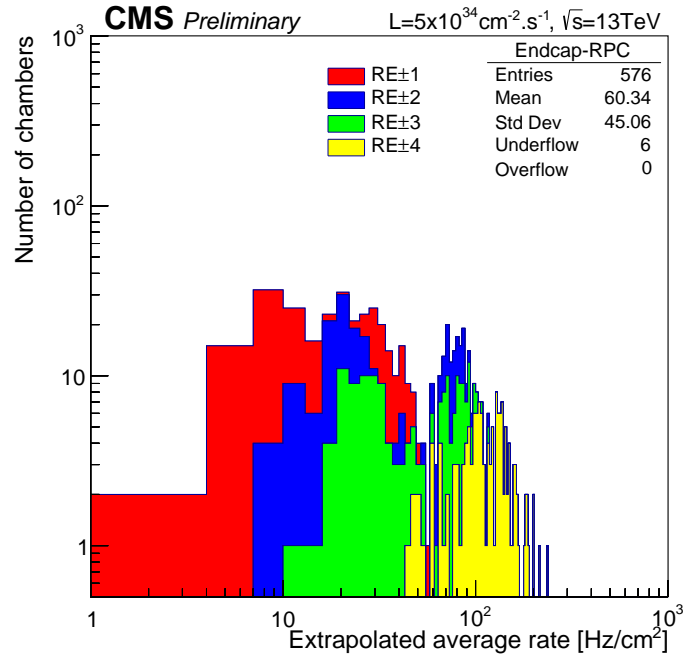
865 Insert a short description of the offline tools : tracking and efficiency algorithm.

866 Identify long term aging effects we are monitoring the rates per strip.

867 **5.3.4 Longevity studies results**



(a)



(b)

Figure 5.1: (5.1a) Extrapolation from 2016 data of single hit rate per unit area in the barrel region. (5.1b) Extrapolation from 2016 data of single hit rate per unit area in the endcap region.

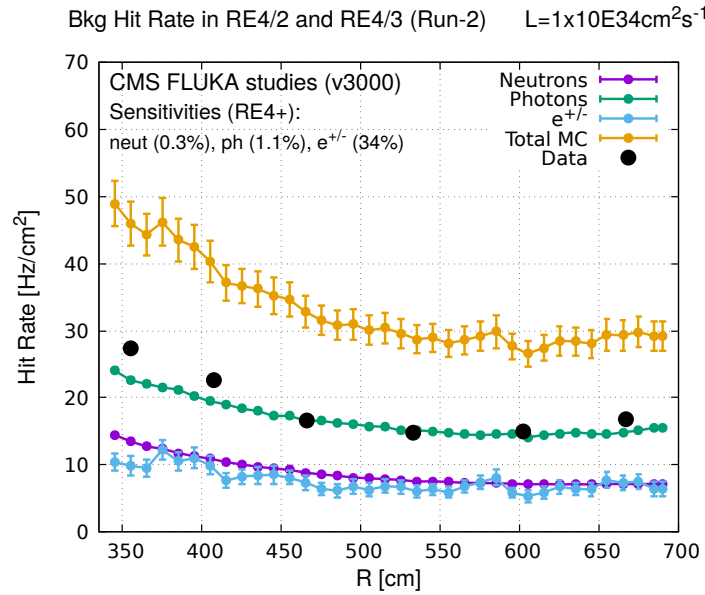


Figure 5.2: Background Fluka simulation compared to 2016 Data at $L = 10^{34} \text{cm}^{-2} \cdot \text{s}^{-1}$ in the fourth endcap disk region. A mismatch in between simulation and data can be observed. [To be understood.]

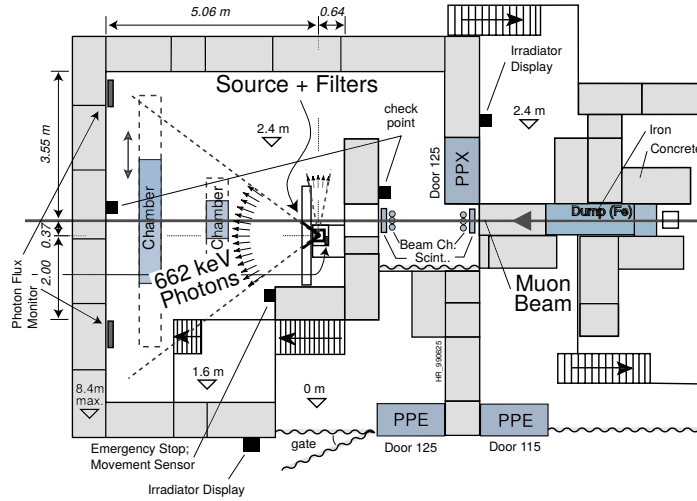


Figure 5.3: Layout of the test beam zone called X5c GIF at CERN. Photons from the radioactive source produce a sustained high rate of random hits over the whole area. The zone is surrounded by 8 m high and 80 cm thick concrete walls. Access is possible through three entry points. Two access doors for personnel and one large gate for material. A crane allows installation of heavy equipment in the area.

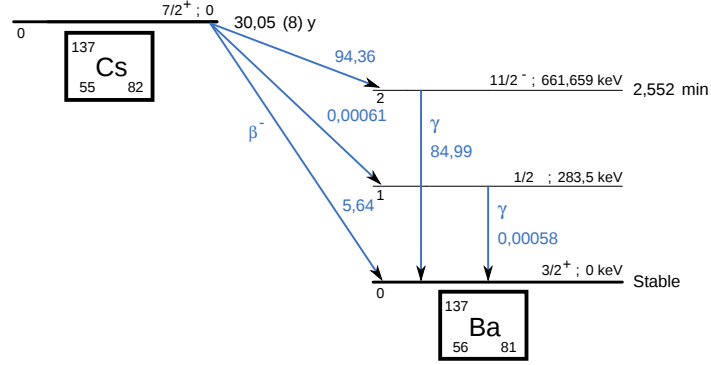


Figure 5.4: ^{137}Cs decays by β^- emission to the ground state of ^{137}Ba ($BR = 5.64\%$) and via the 662 keV isomeric level of ^{137}Ba ($BR = 94.36\%$) whose half-life is 2.55 min.

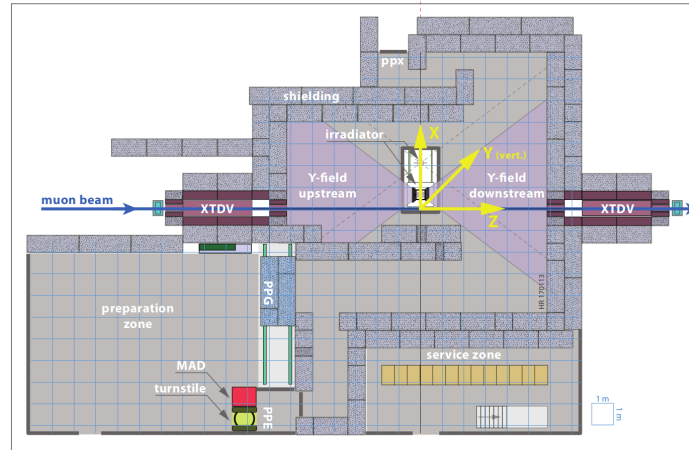


Figure 5.5: Floor plan of the GIF++ facility. When the facility downstream of the GIF++ takes electron beam, a beam pipe is installed along the beam line (z -axis). The irradiator can be displaced laterally (its center moves from $x = 0.65\text{ m}$ to 2.15 m), to increase the distance to the beam pipe.

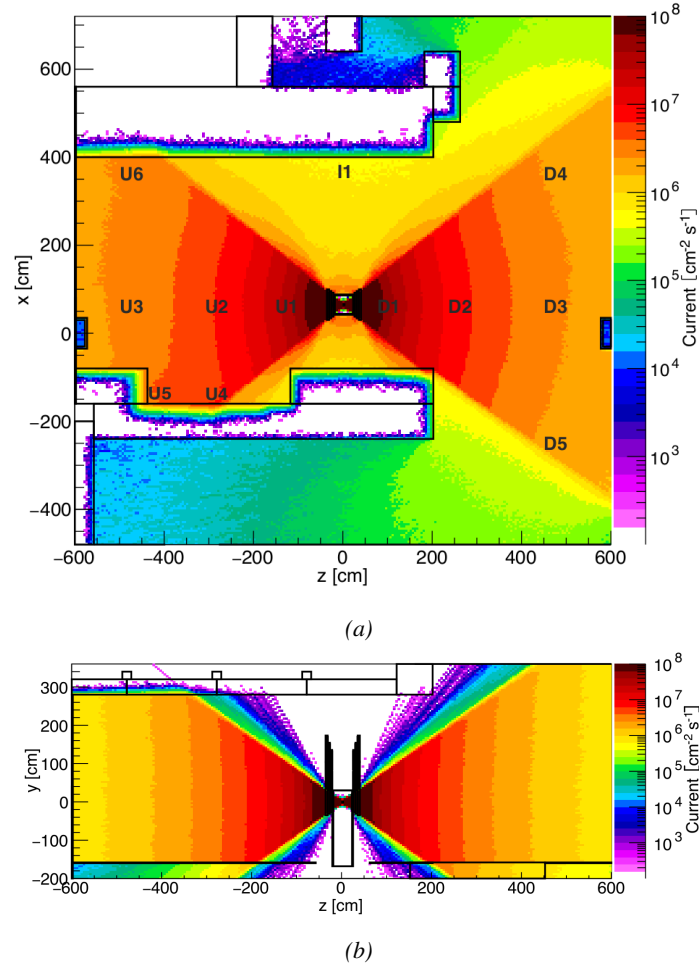


Figure 5.6: Simulated unattenuated current of photons in the xz plane (Figure 5.6a) and yz plane (Figure 5.6b) through the source at $x = 0.65$ m and $y = 0$ m. With angular correction filters, the current of 662 keV photons is made uniform in xy planes.

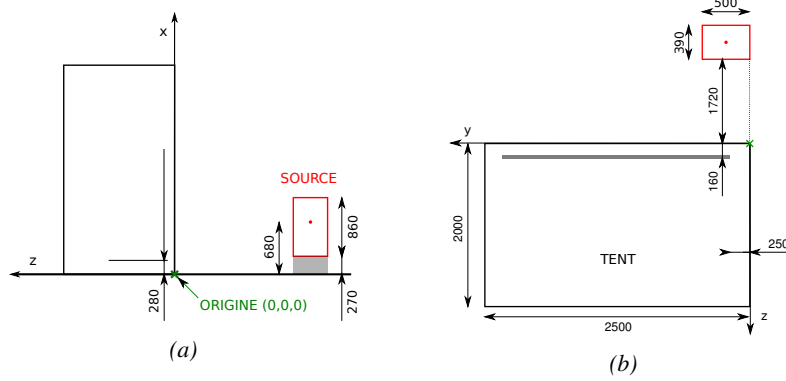


Figure 5.7: Description of the RPC setup. Dimensions are given in mm. A tent containing RPCs is placed at 1720 mm from the source container. The source is situated in the center of the container. RE-4-2-BARC-161 chamber is 160 mm inside the tent. This way, the distance between the source and the chambers plan is 2060 mm. Figure 5.7a provides a side view of the setup in the xz plane while Figure 5.7b shows a top view in the yz plane.

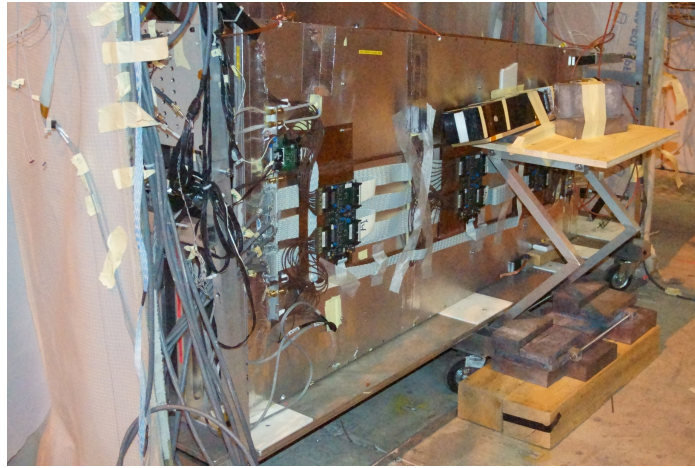


Figure 5.8: RE-4-2-BARC-161 chamber is inside the tent as described in Figure 5.7. In the top right, the two scintillators used as trigger can be seen. This trigger system has an inclination of 10° relative to horizontal and is placed above half-partition B2 of the RPCs. PMT electronics are shielded thanks to lead blocks placed in order to protect them without stopping photons from going through the scintillators and the chamber.

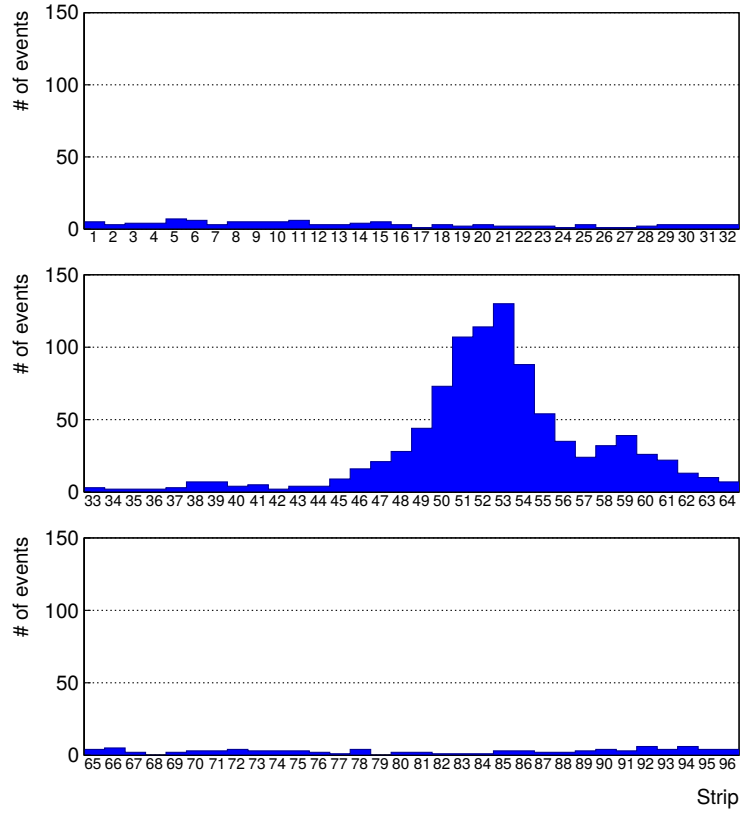


Figure 5.9: Hit distributions over all 3 partitions of RE-4-2-BARC-161 chamber is showed on these plots. Top, middle and bottom figures respectively correspond to partitions A, B, and C. These plots show that some events still occur in other half-partitions than B2, which corresponds to strips 49 to 64, in front of which the trigger is placed, contributing to the inefficiency of detection of cosmic muons. In the case of partitions A and C, the very low amount of data can be interpreted as noise. On the other hand, it is clear that a little portion of muons reach the half-partition B1, corresponding to strips 33 to 48.

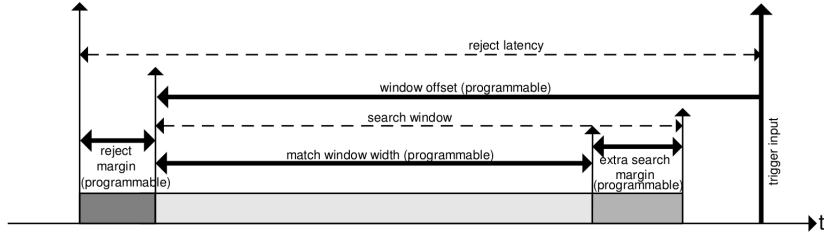


Figure 5.10: Module V1190A Trigger Matching Mode timing diagram.

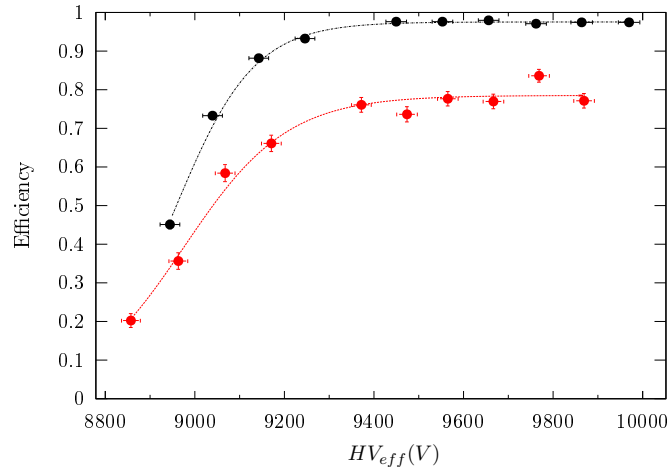
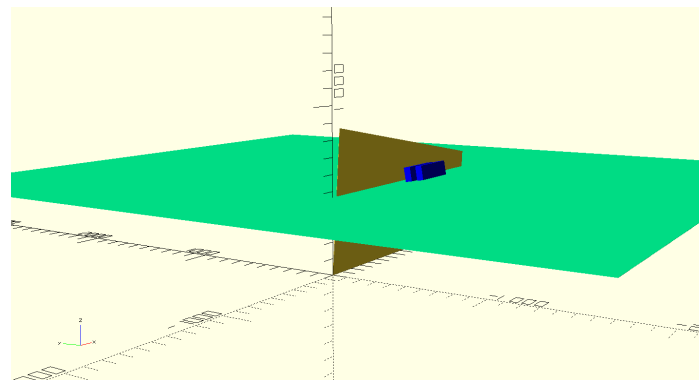
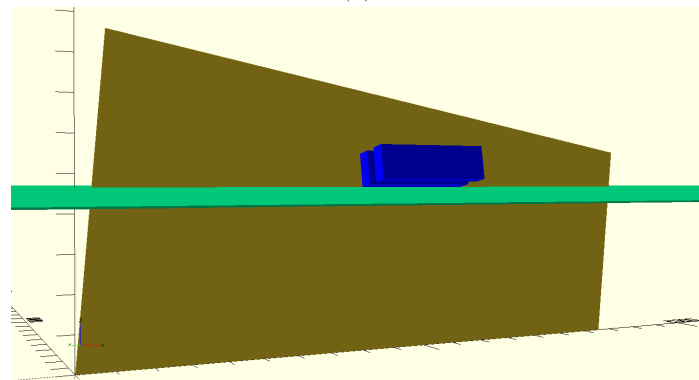


Figure 5.11: Results are derived from data taken on half-partition B2 only. On the 18th of June 2014, data has been taken on chamber RE-2-BARC-161 at building 904 (Preveessin Site) with cosmic muons providing us a reference efficiency plateau of $(97.54 \pm 0.15)\%$ represented by a black curve. A similar measurement has been done at GIF on the 21st of July with the same chamber giving a plateau of $(78.52 \pm 0.94)\%$ represented by a red curve.



(a)



(b)

Figure 5.12: Representation of the layout used for the simulations of the test setup. The RPC is represented as a yellow trapezoid while the two scintillators as blue cuboids looking at the sky. A green plane corresponds to the muon generation plane within the simulation. Figure 5.7a shows a global view of the simulated setup. Figure 5.7b shows a zoomed view that allows to see the 2 scintillators as well as the full RPC plane.

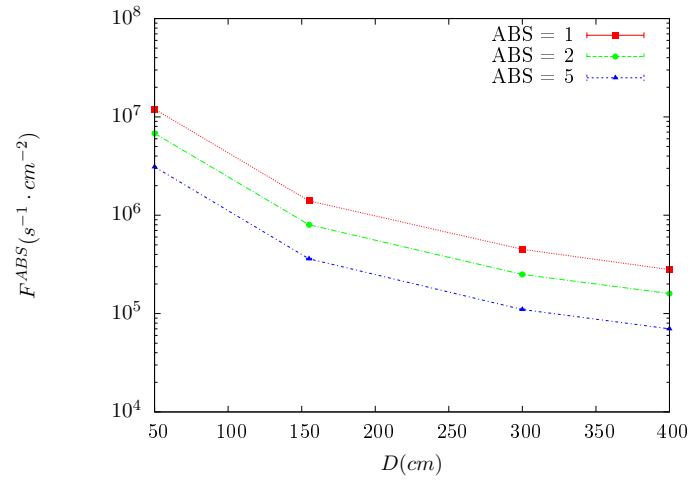


Figure 5.13: γ flux $F(D)$ is plot using values from table 5.1. As expected, the plot shows similar attenuation behaviours with increasing distance for each absorption factors.

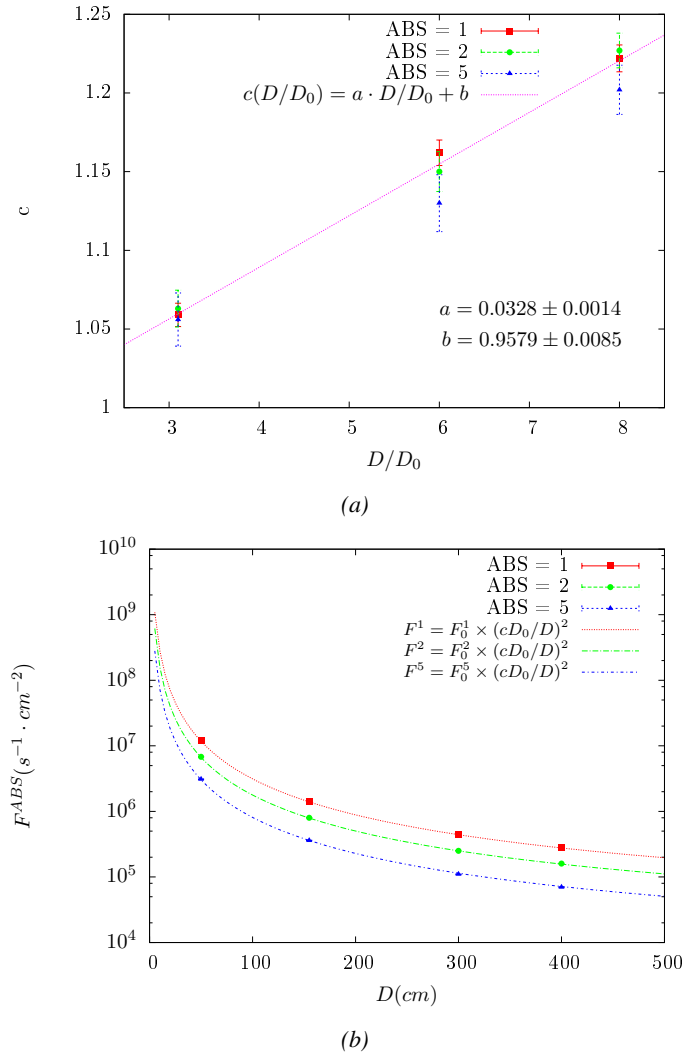


Figure 5.14: Figure 5.14a shows the linear approximation fit done via formulae 5.7 on data from table 5.2. Figure 5.14b shows a comparison of this model with the simulated flux using a and b given in figure 5.14a in formulae 5.4 and the reference value $D_0 = 50cm$ and the associated flux for each absorption factor F_0^{ABS} from table 5.1

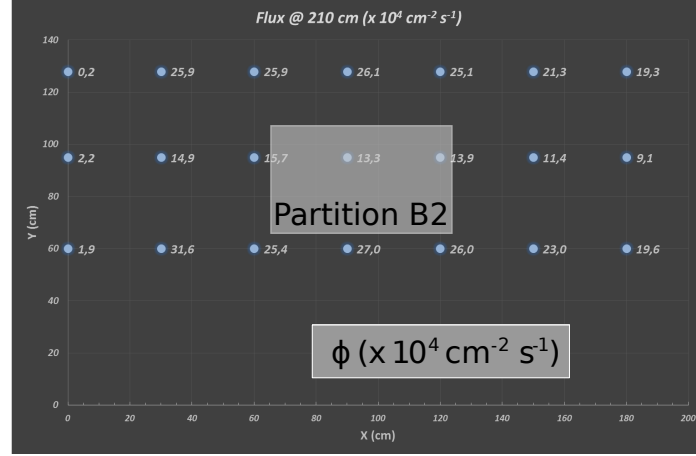


Figure 5.15: Dose measurements has been done in a plane corresponding to the tents front side. This plan is 1900 mm away from the source. As explained in the first chapter, a lens-shaped lead filter provides a uniform photon flux in the vertical plan orthogonal to the beam direction. If the second line of measured fluxes is not taken into account because of lower values due to experimental equipments in the way between the source and the tent, the uniformity of the flux is well showed by the results.

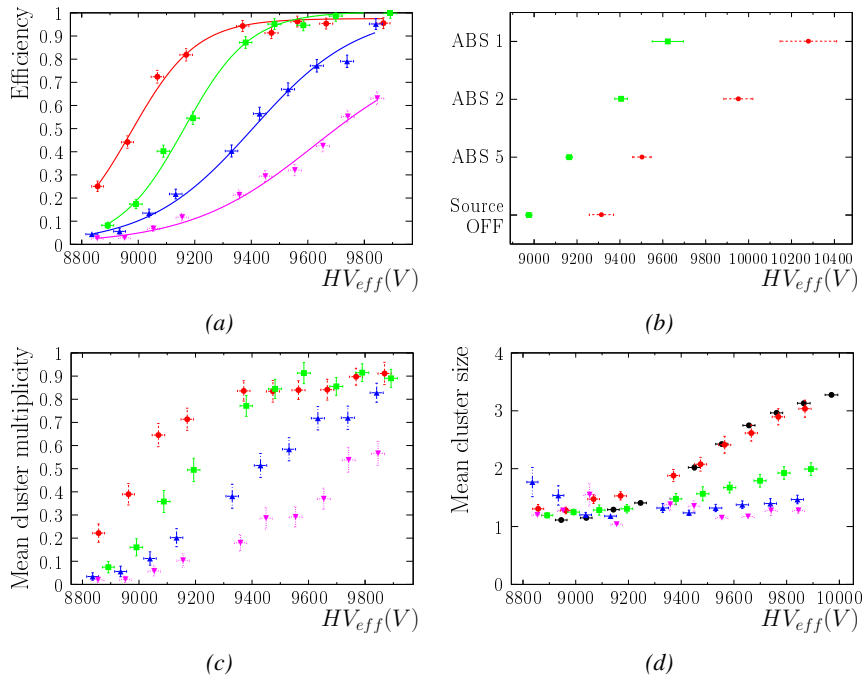


Figure 5.16

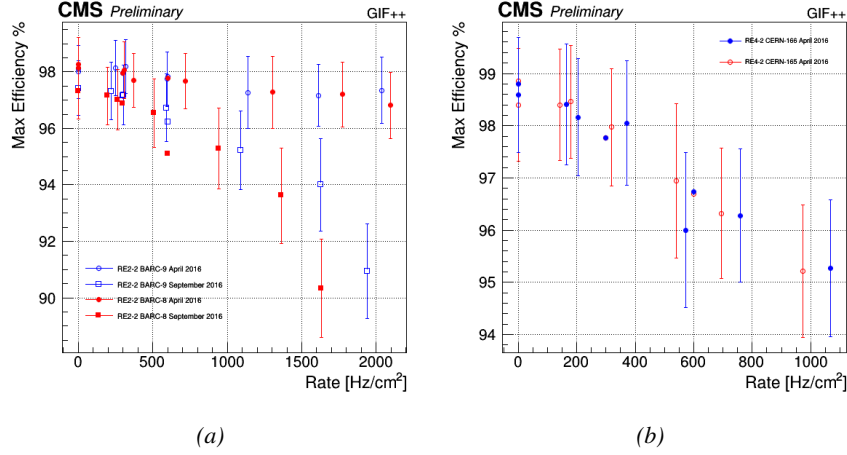


Figure 5.17: Evolution of the maximum efficiency for RE2 (5.17a) and RE4 (5.17b) chambers with increasing extrapolated γ rate per unit area at working point. Both irradiated (blue) and non irradiated (red) chambers are shown.

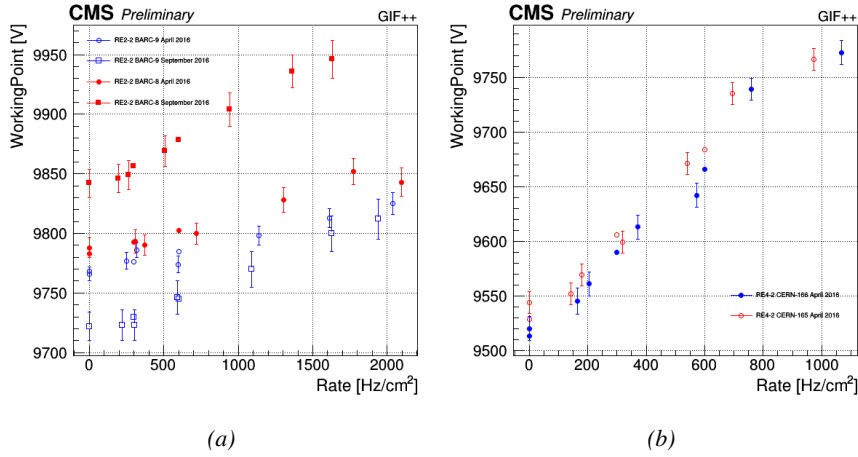


Figure 5.18: Evolution of the working point for RE2 (5.18a) and RE4 (5.18b) with increasing extrapolated γ rate per unit area at working point. Both irradiated (blue) and non irradiated (red) chambers are shown.

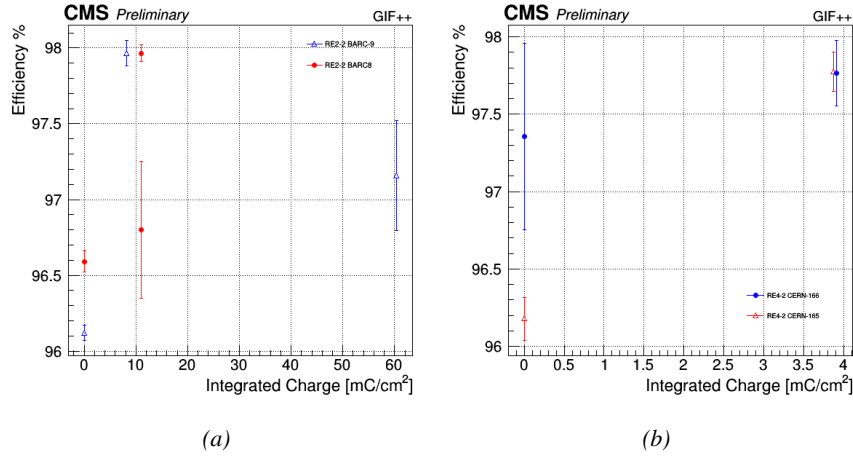


Figure 5.19: Evolution of the maximum efficiency at HL-LHC conditions, i.e. a background hit rate per unit area of 300 Hz/cm², with increasing integrated charge for RE2 (5.19a) and RE4 (5.19b) detectors. Both irradiated (blue) and non irradiated (red) chambers are shown. The integrated charge for non irradiated detectors is recorded during test beam periods and stays small with respect to the charge accumulated in irradiated chambers.

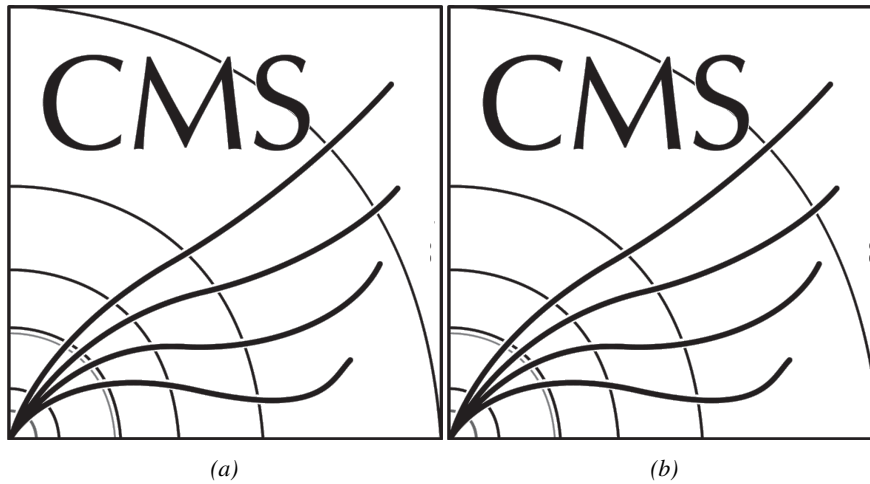


Figure 5.20: Comparison of the efficiency sigmoid before (triangles) and after (circles) irradiation for RE2 (5.20a) and RE4 (5.20b) detectors. Both irradiated (blue) and non irradiated (red) chambers are shown.

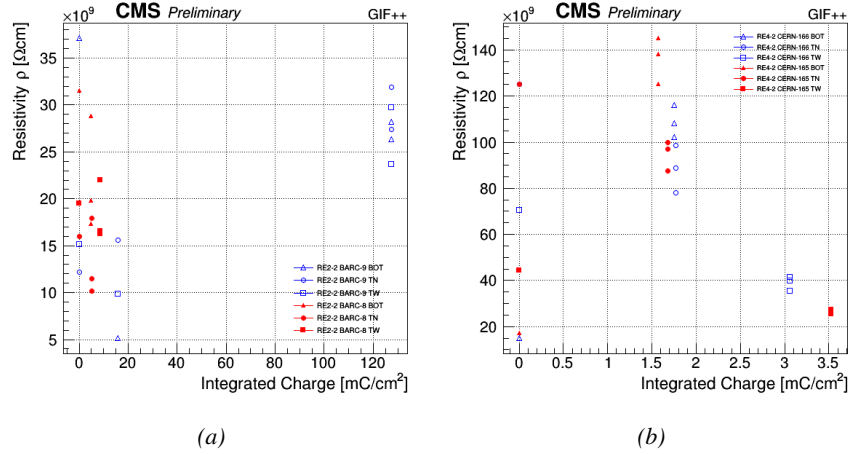


Figure 5.21: Evolution of the Bakelite resistivity for RE2 (5.21a) and RE4 (5.21b) detectors. Both irradiated (blue) and non irradiated (red) chambers are shown.

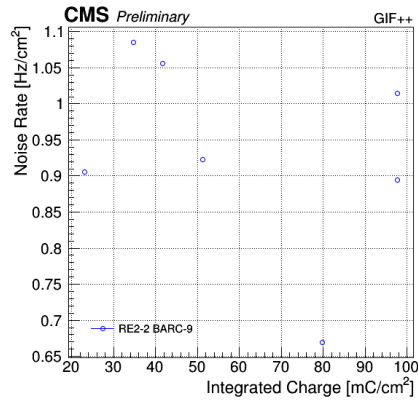


Figure 5.22: Evolution of the noise rate per unit area for the irradiated chamber RE2-2-BARC-9 only.

6

868

869

Investigation on high rate RPCs

870 **6.1 Rate limitations and ageing of RPCs**

871 **6.1.1 Low resistivity electrodes**

872 **6.1.2 Low noise front-end electronics**

873 **6.2 Construction of prototypes**

874 **6.3 Results and discussions**

7

875

876

Conclusions and outlooks

877 **7.1 Conclusions**

878 **7.2 Outlooks**

References

- 880 [1] CERN. Geneva. LHC Experiments Committee. *The CMS muon project :
881 Technical Design Report*. Tech. rep. CERN-LHCC-97-032. CMS Collabora-
882 tion, 1997.
- 883 [2] CERN. Geneva. LHC Experiments Committee. *Technical Proposal for the
884 Phase-II Upgrade of the CMS Detector*. Tech. rep. CERN-LHCC-2015-010.
885 CMS Collaboration, 2015.
- 886 [3] CERN. Geneva. LHC Experiments Committee. *CMS, the Compact Muon
887 Solenoid : technical proposal*. Tech. rep. CERN-LHCC-94-38. CMS Collab-
888 oration, 1994.
- 889 [4] M. Abbrescia et al. “Study of long-term performance of CMS RPC under
890 irradiation at the CERN GIF”. In: *NIMA* 533 (2004), pp. 102–106.
- 891 [5] H.C. Kim et al. “Quantitative aging study with intense irradiation tests for
892 the CMS forward RPCs”. In: *NIMA* 602 (2009), pp. 771–774.
- 893 [6] S. Agosteo et al. “A facility for the test of large-area muon chambers at high
894 rates”. In: *NIMA* 452 (2000), pp. 94–104.
- 895 [7] PoS, ed. *CERN GIF ++ : A new irradiation facility to test large-area par-
896 ticle detectors for the high-luminosity LHC program*. Vol. TIPP2014. 2014,
897 pp. 102–109.
- 898 [8] CAEN. *Mod. V1190-VX1190 A/B, 128/64 Ch Multihit TDC*. 13th ed. 2012.
- 899 [9] M. Abbrescia et al. “Cosmic ray tests of double-gap resistive plate chambers
900 for the CMS experiment”. In: *NIMA* 550 (2005), pp. 116–126.



901

902

903

A data acquisition software for VME CAEN TDCs

904

905

906

907

908

909

Certifying detectors in the perspective of HL-LHC required to develop tools for the GIF++ experiment. One of them was the Data Acquisition (DAQ) software that allows to make the communications in between the computer and the TDC modules in order to retrieve the RPC data. In this appendix, details about the software, as of how the software was written, how it functions and how it can be exported to another similar setup.

910

A.1 Introduction

B

911

912

Details on the online analysis package

913

B.1 Introduction

914

insert text here



915

916

917

Structure of the hybrid simulation software

918 **C.1 Introduction**

919 insert text here...

